PNAS RESEARCH ARTICLE | APPLIED BIOLOGICAL SCIENCES OPEN ACCESS

Fluorinated macromolecular amphiphiles as prototypic molecular drones

Yujie Zheng[a,b,1], Lijun Zhu[a,1], Changsheng Ke[a,b,1], Yu Li[a], Zhiwen Zhou[b], Mou Jiang[c], Fang Wang[a], Pei He[a], Xin Zhou[a,d], Zhong-Xing Jiang[a,d,e,2], and Shizhen Chen[a,d,2]

Affiliations are included on p. 9.

Edited by David Weitz, Harvard University, Cambridge, MA; received March 21, 2024; accepted July 14, 2024

The advent of drones has revolutionized various aspects of our lives, and in the realm of biological systems, molecular drones hold immense promise as "magic bullets" for major diseases. Herein, we introduce a unique class of fluorinated macromolecular amphiphiles, designed in the shape of jellyfish, serving as exemplary molecular drones for fluorine-19 MRI (^{19}F MRI) and fluorescence imaging (FLI)-guided drug delivery, status reporting, and targeted cancer therapy. Functioning akin to their mechanical counterparts, these biocompatible molecular drones autonomously assemble with hydrophobic drugs to form uniform nanoparticles, facilitating efficient drug delivery into cells. The status of drug delivery can be tracked through aggregation-induced emission (AIE) of FLI and ^{19}F MRI. Furthermore, when loaded with a heptamethine cyanine fluorescent dye IR-780, these molecular drones enable near-infrared (NIR) FL detection of tumors and precise delivery of the photosensitizer. Similarly, when loaded with doxorubicin (DOX), they enable targeted chemotherapy with fluorescence resonance energy transfer (FRET) FL for real-time status updates, resulting in enhanced therapeutic efficacy. Compared to conventional drug delivery systems, molecular drones stand out for their simplicity, precise structure, versatility, and ability to provide instantaneous status updates. This study presents prototype molecular drones capable of executing fundamental drone functions, laying the groundwork for the development of more sophisticated molecular machines with significant biomedical implications.

molecular drones | fluorinated macromolecular amphiphiles | drug delivery | multimodal imaging | self-assemble

Significance

Learning from nature and the real world, we have developed a fluorinated macromolecular amphiphile with a jellyfish shape and all the basic functions of a drone, including cargo loading and release, status reporting, remote tracking, and targeting, whose capabilities as a prototypical molecular drone have been elegantly demonstrated in vitro and in mice by loading photosensitizer for dual-modal imaging detection of tumor and loading chemotherapy drug for targeted cancer therapy. Its easy availability, high biocompatibility, precise structure, and versatility lay a firm foundation for more sophisticated molecular drones of biomedical importance and shed light on regular theranostic systems that are usually too complicated to replicate and too complex for clinical translation.

In recent years, drones have seen widespread adoption across various applications such as cargo delivery, surveillance, and combat, profoundly transforming human capabilities. In the field of biomedicine, the concept of molecular drones has emerged, aiming to serve as precise "magic bullets" for accurate diagnosis, targeted drug delivery, and personalized therapy of major diseases (1–5). While polymer-based drug delivery systems have shown promise in diagnostics, therapeutics, and theranostics (6–10), their inherent polydispersity, structural complexity, and difficulty in precise manipulation hinder their potential as molecular drones (11–14). Hence, the development of macromolecules with precise structure, stimuli-responsiveness, and multifunctionality holds great promise for molecular drones.

When designing biomedical molecular drones, it is crucial to incorporate essential drone functions. First, in vivo imaging systems play a pivotal role in status reporting and decision-making. While fluorescence imaging (FLI) offers convenience and high sensitivity (15–19), it is limited by tissue depth and autofluorescence (20–22). On the other hand, ^{19}F MRI provides quantitative images without tissue depth limitations or background interference. Their combination offers an ideal information system for molecular drones, enabling convenient FLI of cells and superficial tissues, alongside "hot-spot" ^{19}F MRI imaging of the entire body (23–27), akin to the short-range vision and long-range radio systems in drones. Second, cargo loading, delivery, and release capabilities are paramount. In the absence of remote-controlled mechanical systems, molecular drones can initiate actions through local stimuli like hydrophobic interactions and pH or external stimuli such as light and heat (28–31). Third, targeting capability is crucial, particularly in cancer diagnosis and therapy. While the enhanced permeability and retention (EPR) effect offers passive targeting by self-assembling into nanoparticles (32–34), incorporating active targeting motifs like antibodies and aptamers (35–37) can complicate synthesis and functionality. Finally, high biocompatibility, stability, low immunogenicity, and prolonged blood circulation time are prerequisites. Therefore, it is imperative to integrate these functions and properties into molecular drones through meticulous design and precise synthesis.

Author contributions: X.Z., Z.-X.J., and S.C. designed research; Y.Z., L.Z., C.K., Y.L., Z.Z., M.J., F.W., and P.H. performed research; Z.Z. contributed new reagents/analytic tools; Y.Z. and L.Z. analyzed data; and Y.Z., L.Z., and Z.-X.J. wrote the paper.

The authors declare no competing interest.

This article is a PNAS Direct Submission.

[1]Y.Z., L.Z., and C.K. contributed equally to this work.

[2]To whom correspondence may be addressed. Email: zxjiang@apm.ac.cn or chenshizhen@wipm.ac.cn.

This article contains supporting information online at https://www.pnas.org/lookup/suppl/doi:10.1073/pnas.2405877121/-/DCSupplemental.

Published August 20, 2024.

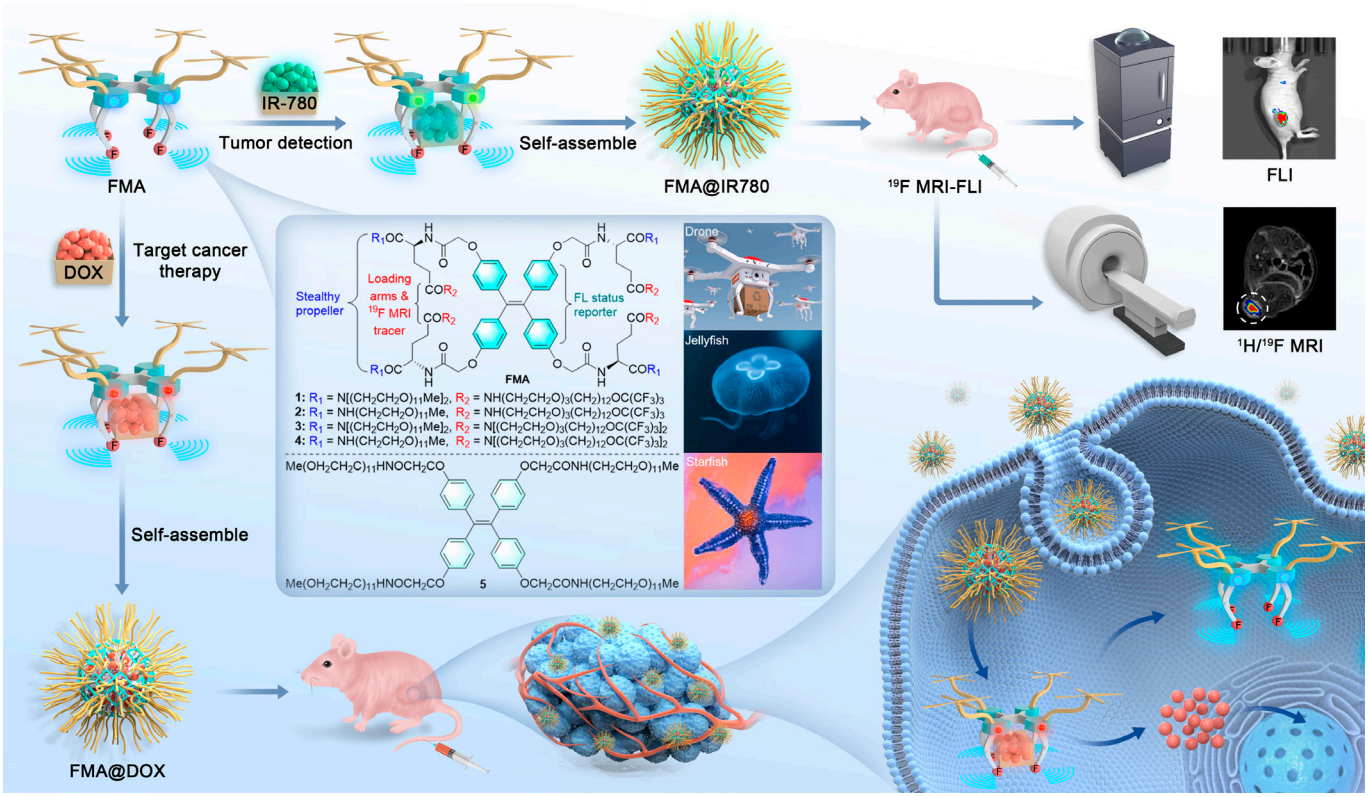

Fig. 1. Schematic illustration of FMA **1**-**4** with a jellyfish shape as prototypical molecular drones for ^{19}F MRI-FLI-guided drug delivery, status reporting, tumor detection, and targeted cancer therapy.

Herein, we introduce a series of fluorinated macromolecular amphiphiles (FMA **1-4**) in a jellyfish shape as prototypical molecular drones for ^{19}F MRI-FLI-guided drug delivery, status reporting, and targeted cancer therapy (Fig. 1). With environment-sensitive AIE FL (38, 39), tetraphenyl ethylene (TPE) serves as a real-time status reporter and multivalence backbone. Amphiphilic side chains comprising hydrophobic 12-perfluoro-*tert*-butoxyl-1-dodecoxyl (PFTB-DC) tails and hydrophilic monodisperse polyethylene glycol (M-PEG) heads, assembled on L-glutamic acid backbones, provide basic drone functionalities. The PFTB-DC tails act as imaging-traceable loading arms, utilizing perfluoro-*tert*-butoxy (PFTB) groups for ^{19}F MRI signal and DC tails for self-assembly and drug loading. Meanwhile, M-PEGs serve as drone propellers, enhancing solubility, mobility, blood circulation time, and immune evasion (40–42). To optimize physicochemical properties and performance, FMA **1-4** are equipped with different hydrophilic heads and hydrophobic tails. Additionally, a starfish-shaped hydrophilic TPE **5** serves as a control to elucidate the structure–function relationship (43). Hence, jellyfish-shaped FMA **1-4**, equipped with ^{19}F MRI-FLI communication systems, PFTB-DC loading arms, and M-PEG propellers, are poised to perform fundamental molecular drone actions.

Results and Discussion

With these principles in mind, the synthesis of FMA **1-4** was efficiently achieved from azides **6** and **7** through a streamlined six-step process, yielding 30 to 42% overall (*SI Appendix*, Scheme S1). The hydrophilic heads, M-PEG amines **8** and **10**, as well as the hydrophobic tails, PFTB-DC amines **9** and **11**, were synthesized via either Staudinger reduction or reductive dimerization of the corresponding azides **6** and **7** (44–47) (*SI Appendix*). Following this, amines **8** and **10** were conjugated to the carboxyl group of a commercially available L-glutamic acid derivative **12**, yielding the respective amides **13** and **14**. Subsequent treatment with trifluoroacetic acid removed the *tert*-butyl protecting group, allowing coupling with amines **9** and **11** to yield the corresponding amides **17-20**. Removal of the fluorenylmethyloxycarbonyl (Fmoc) protecting group in amides **17-20** was followed by conjugation of resulting amines **21-24** to TPE tetra-acid **25**, simultaneously forming four amide bonds in one pot, thus providing FMA **1-4** on multi-hundred-milligram scales (*SI Appendix*, Scheme S2). The structures of FMA **1-4** were confirmed by ^{1}H/^{13}C/^{19}F NMR and MALDI-TOF mass spectra (*SI Appendix*).

Using TPE **5** as a control, the physicochemical properties of FMA **1-4** were initially examined. Featuring multiple hydrophilic M-PEGs, FMA **1-4** exhibited high water solubilities (>130 g/L), with water-octanol partition coefficients (LogP) revealing that higher PFTB-DCs/M-PEGs ratios (P/M ratio, the branch number ratio of hydrophobic PFTB-DCs tails to hydrophilic M-PEG heads in FMA **1-4**) corresponded to increased lipophilicity (Fig. 2*A*). Conversely, nearly identical lipophilicities were observed for all TPE amphiphiles lacking L-glutamic acid scaffolds and PFTB groups (43), underscoring the substantial impact of molecular size on the lipophilicity of such TPE amphiphiles. Relative to TPE **5**, FMA **1-4** displayed slight red-shifted UV absorption in water (Fig. 2*B*), with molar extinction coefficient (ε) measurements indicating that higher P/M ratios correlated with enhanced light absorption (Fig. 2*C*). While FMA **1-4** emitted weak FL in methanol, they exhibited up to a 10.6-fold increase in FL intensity in water (Fig. 2 *D*–*H*), highlighting the significant AIE FL induced by the hydrophobic PFTB-DC side chains. Consequently, FMA **1-4** demonstrated relative FL quantum yields (ϕ) up to 15.1-fold higher than TPE **5** (Fig. 2*I*). The combination of high water solubility and P/M ratio-dependent lipophilicity, UV absorption, and AIE FL underscores the potential for optimizing molecular drones through structure modification.

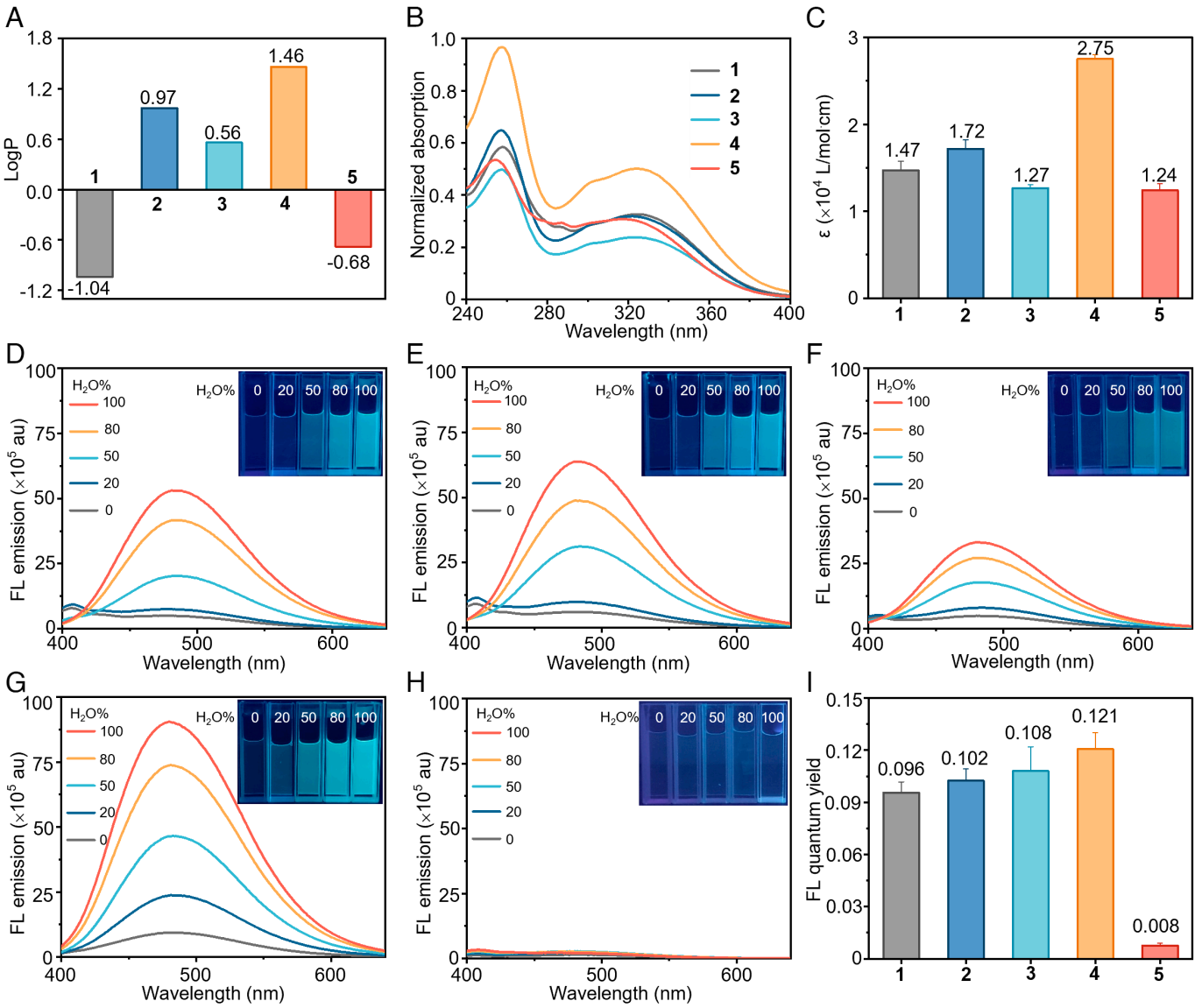

Fig. 2. LogP (*A*), UV absorption spectra in water (*B*), molar extinction coefficients in water (*C*), solvent-dependent FL emission spectra with inset photos of solutions under a 365 nm UV lap (*D*: **1**, *E*: **2**, *F*: **3**, *G*: **4**, *H*: **5**, at 50 μM, λ_{ex} = 330 nm, solvent changed from methanol to water), relative FL quantum yield in water (*I*) of FMA **1-4** and TPE **5**.

The self-assembly behavior of FMA **1-4** in water was investigated to elucidate the collective behavior of the molecular drones. Initially, upon solvent transition from methanol to water, significant broadening and upfield shift of the ^{19}F NMR peaks of FMA **1-4** indicated restricted mobility and the formation of a hydrophobic environment around the PFTB groups in water (48, 49) (Fig. 3*A*). Additionally, reduced cross-peaks between the M-PEGs and PFTB-DCs in the ^{1}H–^{1}H ROESY spectrum provided evidence for ordered aggregate formation in water with PFTB-DCs and M-PEGs aggregating into hydrophobic and hydrophilic phases, respectively, rather than M-PEG and PFTB-DCs tangled together with additional cross-peaks in methanol (*SI Appendix*, Fig. S1). Furthermore, FMA **1-4** exhibited concentration-dependent FL in water, manifesting in three distinct states (Fig. 3*B*), suggesting a shift in the aggregation mode of the TPE core with changing concentrations. Subsequent investigations employing Nile Red as a hydrophobic fluorescence cargo revealed nearly identical critical micelle concentrations (CMCs) around 10 μM for FMA **1-4** (50), despite their structural differences (Fig. 3*C*). This observation suggests a minor role of the side chains in determining their CMCs. Moreover, dynamic light scattering (DLS) analysis of the aggregates showcased a transition from heterogeneous small particles to relatively monodisperse larger ones with increasing concentrations. Correspondingly, transmission electron microscopy (TEM) images depicted a shift from heterogeneous loose nanoparticles to homogeneous compact ones with higher P/M ratios (Fig. 3 *D–F* and *SI Appendix*, Figs. S2 *a–i*). In contrast, hydrophilic TPE **5** solely aggregated into spherical nanoparticles (*SI Appendix*, Figs. S2 *j–l*). Consequently, propelled by the hydrophobic PFTB-DC tails, FMA **1-4** exhibit a propensity for self-assembly into concentration-dependent aggregates with AIE FL status reporting, akin to orchestrating teams based on the number of drones present.

In addition to their status-reporting AIE FLI capabilities, FMA **1-4** have multiple ^{19}F for susceptible "hot spot ^{19}F MRI. A sharp singlet ^{19}F NMR peak was observed, originating from 36 or 72 equivalent ^{19}F (Fig. 3*A*), effectively circumventing chemical shift imaging artifacts and significantly enhancing ^{19}F MRI sensitivity. Furthermore, the short longitudinal relaxation times (T_1, about 620 ms) and appropriate transverse relaxation times (T_2, about

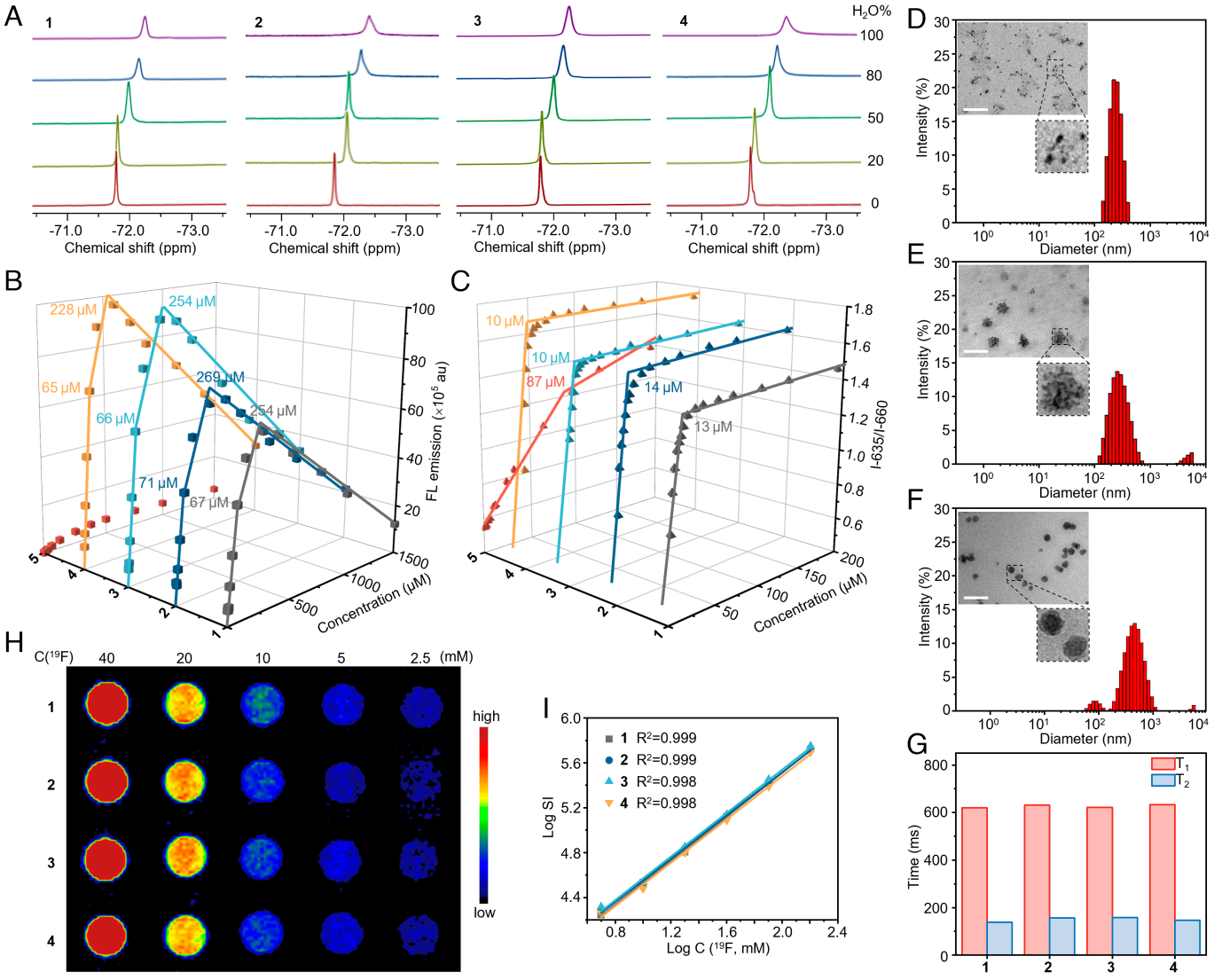

Fig. 3. Partial solvent-dependent ^{19}F NMR spectra of FMA **1-4** (*A*), plot of maximum FL intensity versus the concentration (*B*) and plot of Nile Red FL intensity ratios between 635 nm and 660 nm versus the concentration (*C*) of FMA **1-4** and TPE **5**, DLS with inset TEM images (*D*: 5 μM, *E*: 100 μM, *F*: 1,000 μM, scale bar: 200 nm) of FMA **2**, ^{19}F relaxation times (*G*: 278 μM in water), ^{19}F MRI phantom images at the indicated ^{19}F concentrations (*H*), and plot of the logarithm of the ^{19}F MRI signal intensity, Log SI, versus the logarithm of the ^{19}F concentration, Log C(^{19}F), of FMA **1-4** (*I*). The corresponding figures for FMA **1**, **3** and TPE **5** can be found in *SI Appendix*.

140 ms) of FMA **1-4** (Fig. 3*G*) ensured a high signal-to-noise ratio (SNR) for ^{19}F MRI within the same acquisition time (51, 52). Remarkably, with a brief data acquisition time of only 8 min, FMA **1-4** yielded clear images with a low detectable ^{19}F concentration of 2.5 mM (Fig. 3*H*). In terms of detectable molecular concentrations, the values of 70 μM for FMA **1**, **2**, and 35 μM for FMA **3**, **4** fall within the range of in vivo drug concentrations, thus enabling the tracking of drug-loaded FMA **1-4** in vivo. Moreover, for FMA **1-4**, the logarithm of the ^{19}F MRI signal intensity (SI) demonstrated a perfect proportionality to the logarithm of the ^{19}F concentration (Fig. 3*I*), facilitating the quantification of FMA **1-4** via ^{19}F MRI. Therefore, FMA **1-4** exhibit the ability to generate both status-reporting FLI and sensitive, quantitative "hot spot" ^{19}F MRI, making them an ideal imaging system for molecular drones.

Following the exploration of the imaging system, the biocompatibility of FMA **1-4** was assessed across various human cell lines using the CCK-8 cytotoxicity assay, encompassing lung cancer A549 cells, breast cancer MCF-7 cells, and normal breast MCF-10A cells. Surprisingly, FMA **1-4** exhibited P/M ratio-dependent cytotoxicity, with biocompatibility increasing with higher P/M ratios [**1** (1/2) < **3** (2/2) < **2** (1/1) < **4** (2/1), Fig. 4 *A*–*C*]. Interestingly, FMA **3**, containing more M-PEG, displayed significantly higher cytotoxicity than FMA **4**, contrary to the common expectation that more PEGs would induce less cytotoxicity. However, this cytotoxicity trend aligns with previous observations of TPE amphiphiles (43), suggesting a consistent trend among such compounds. In contrast, TPE **5** contains only hydrophilic M-PEGs, exhibited reduced cellular uptake, and enhanced biosafety, resulting in negligible cytotoxicity of TPE **5**. Additionally, a hemolysis assay revealed no significant hemolysis (<5%) for up to 160 μM of FMA **1-3** and slight hemolysis (<10%) for FMA **4** (Fig. 4*D*). In comparison, TPE **5** showed no apparent cytotoxicity or hemolysis. Furthermore, the uptake of FMA **1-4** by MCF-7 cells was investigated. Confocal microscopy images revealed strong FL of FMA **1-4** in the cytoplasm (Fig. 4*E*). Semiquantitative analysis demonstrated a significantly higher uptake of FMA **1** compared to FMA **2-4** in each cell (*SI Appendix*, Fig. S3), suggesting that cytotoxicity may be related to cell uptake. The structure-biocompatibility relationship study unveiled the critical role of the P/M ratio in cytotoxicity and cell uptake, which holds significance for the design of biocompatible TPE amphiphiles.

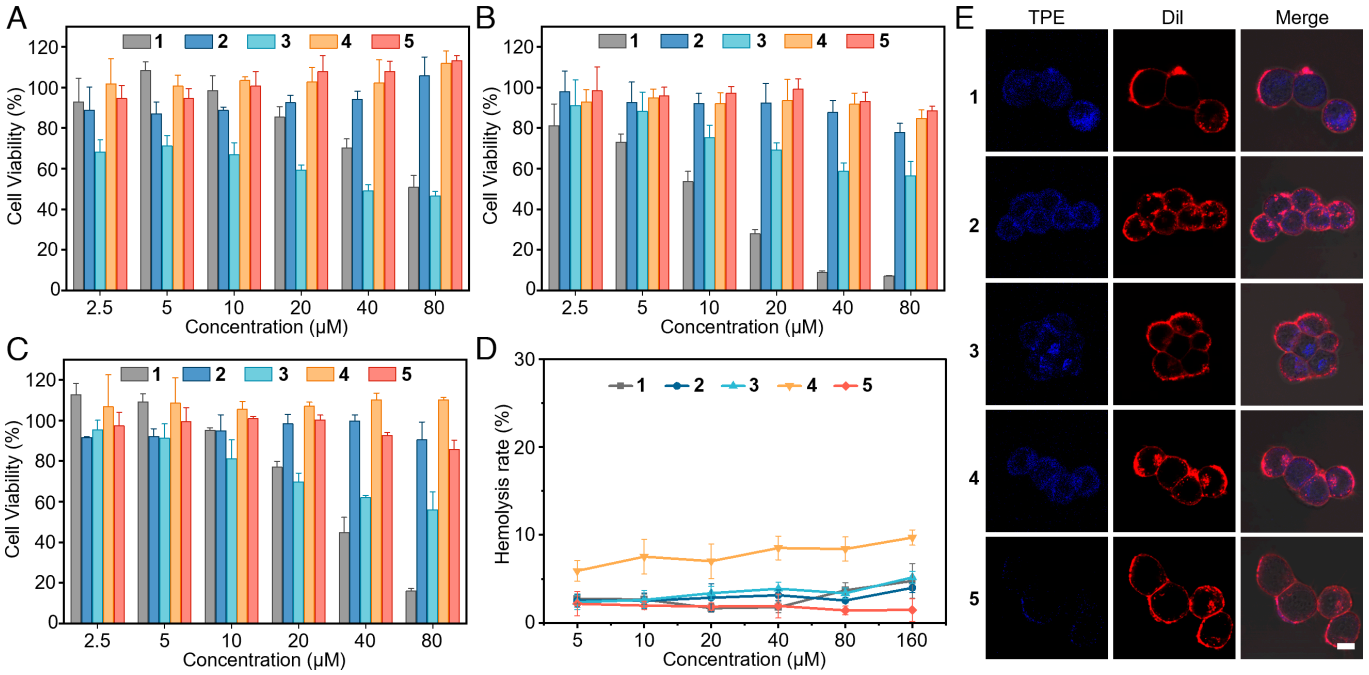

Fig. 4. Cytotoxicity assay of FMA **1-4** and TPE **5** in A549 cells (*A*), MCF-7 cells (*B*), and MCF-10A cells (*C*). Hemolysis assay of FMA **1-4** and TPE **5** with deionized water and PBS as controls (*D*). Confocal microscopy images of MCF-7 cells after incubation with 10 μM of FMA **1-4** and TPE **5** for 24 h (*E*, scale bar: 10 μm).

With its convenient synthesis, high FLI, and ^{19}F MRI capabilities, as well as high biocompatibility, FMA **2** emerged as an exemplary molecular drone for ^{19}F MRI-FLI dual imaging-guided drug delivery, status reporting, and cancer therapy. First, the photosensitizer IR-780, emitting near-infrared FL (NIR FL), was chosen as a model drug to facilitate ^{19}F MRI-NIR FLI dual-modal status reporting and tumor detection. IR-780 was efficiently loaded onto FMA **2** using the solvent evaporation method (53), yielding monodisperse spherical nanoparticles **FMA@IR780** with a size of 183 nm and a polydispersity (PDI) of 0.21 (Fig. 5*A*). The entrapment efficiency and loading content of IR-780 in **FMA@IR780** were measured as 95.5% and 3.7%, respectively, using an HPLC method. DLS monitoring revealed the high stability of **FMA@IR780** over 7 d (*SI Appendix*, Fig. S4*A*). Furthermore, **FMA@IR780** emitted strong red-shifted NIR FL around 800 nm (Fig. 5*B*). With a sharp singlet ^{19}F NMR peak, **FMA@IR780** also exhibited sensitive and quantitative ^{19}F MRI, achieving a low ^{19}F concentration of 2.5 mM (Fig. 5*C* and *SI Appendix*, Fig. S5*A*), demonstrating its ^{19}F MRI-FLI dual imaging capability. The biocompatibility of **FMA@IR780** was evaluated in A549 cells, and **FMA@IR780** showed similar cytotoxicity compared to the free IR-780 (*SI Appendix*, Fig. S6*A*). Subsequently, ^{19}F NMR and NIR FL were utilized to monitor the uptake of **FMA@IR780** by A549 cells. A singlet ^{19}F NMR peak was detected in **FMA@IR780**-treated A549 cells (Fig. 5*D*), indicating the uptake of **FMA@IR780**, with approximately 1.3×10^{-8} μM FMA **2** taken up by each cell. Additionally, confocal microscope images revealed the colocalized FL of FMA **2** and IR-780 in the cytoplasm, indicating that **FMA@IR780** was taken up and remained intact in the cells (Fig. 5*E*). Therefore, FMA **2** can efficiently load IR-780 into monodisperse and stable nanoparticles **FMA@IR780** and deliver IR-780 into A549 cells, which can be conveniently and quantitatively monitored by ^{19}F NMR and FL.

The investigation into ^{19}F MRI-NIR FLI dual-modal status reporting and tumor detection with **FMA@IR780** was further extended to mice. First, at an FMA **2** dose of 27 mg/kg, no signs of toxicity or tissue abnormality were observed in BALB/c nude mice over 14 d following intravenous injection of **FMA@IR780**, underscoring its high biocompatibility. Second, upon intravenous administration of **FMA@IR780** to BALB/c nude mice bearing xenograft A549 lung tumors of approximately 200 mm^3, whole-body NIR FLI revealed the gradual accumulation of **FMA@IR780** in the tumor, reaching maximum NIR FL intensity around the 24th hour (Fig. 5 *F* and *G*). Strong NIR FL persisted in the tumor up to 72 h postinjection, offering an extended time window for tracking **FMA@IR780** and monitoring tumor dynamics. NIR FLI of the internal organs and tumors collected 24 h postinjection demonstrated the high tumor-targeting capability of **FMA@IR780** (Fig. 5 *H* and *I*). Third, ^{19}F MRI depicted the accumulation of **FMA@IR780** in the tumor region, with maximum ^{19}F MRI signal intensity observed around the 24th hour (Fig. 5*J* and *SI Appendix*, Figs. S7 and S8), showing excellent agreement with NIR FLI results. Therefore, leveraging IR-780 as a model drug, the molecular drone system **FMA@IR780** showcased convenient drug loading and ^{19}F MRI-NIR FLI dual imaging-guided delivery in cancer cells and tumor-bearing mice. These findings offer unique molecular drone strategies for sensitive multimodal imaging detection of tumors, tumor-targeted drug delivery, and potential imaging-guided cancer PDT.

With the robust targeting capabilities of the molecular drone delivery system, we successfully loaded the chemotherapy drug DOX onto FMA **2**, enabling ^{19}F MRI-NIR FLI dual imaging-guided cancer therapy. Initially, we obtained a series of DOX-loaded nanoparticles at various DOX/FMA **2** molar ratios (0/4, 1/4, 2/4, 3/4, and 4/4). Among these formulations, **FMA@DOX** with a molar ratio of 4/4 exhibited a monodisperse spherical structure approximately 126 nm in size, demonstrating remarkable stability over 14 d without significant changes in particle size and PDI (Fig. 6*A* and *SI Appendix*, Fig. S4*B*). Moreover, with an increase in the DOX loading ratio, both the Zeta potential and the absorption of DOX at 480 nm of the nanoparticles increased (Fig. 6 *B* and *C*), indicating successful DOX loading. Subsequently, under excitation with a 330 nm laser, the FL emission of FMA **2** at 480 nm decreased proportionally with the DOX content, while the FL emission of DOX at 590 nm increased (Fig. 6*D*). This observed phenomenon pointed to a FRET between FMA **2** and DOX,

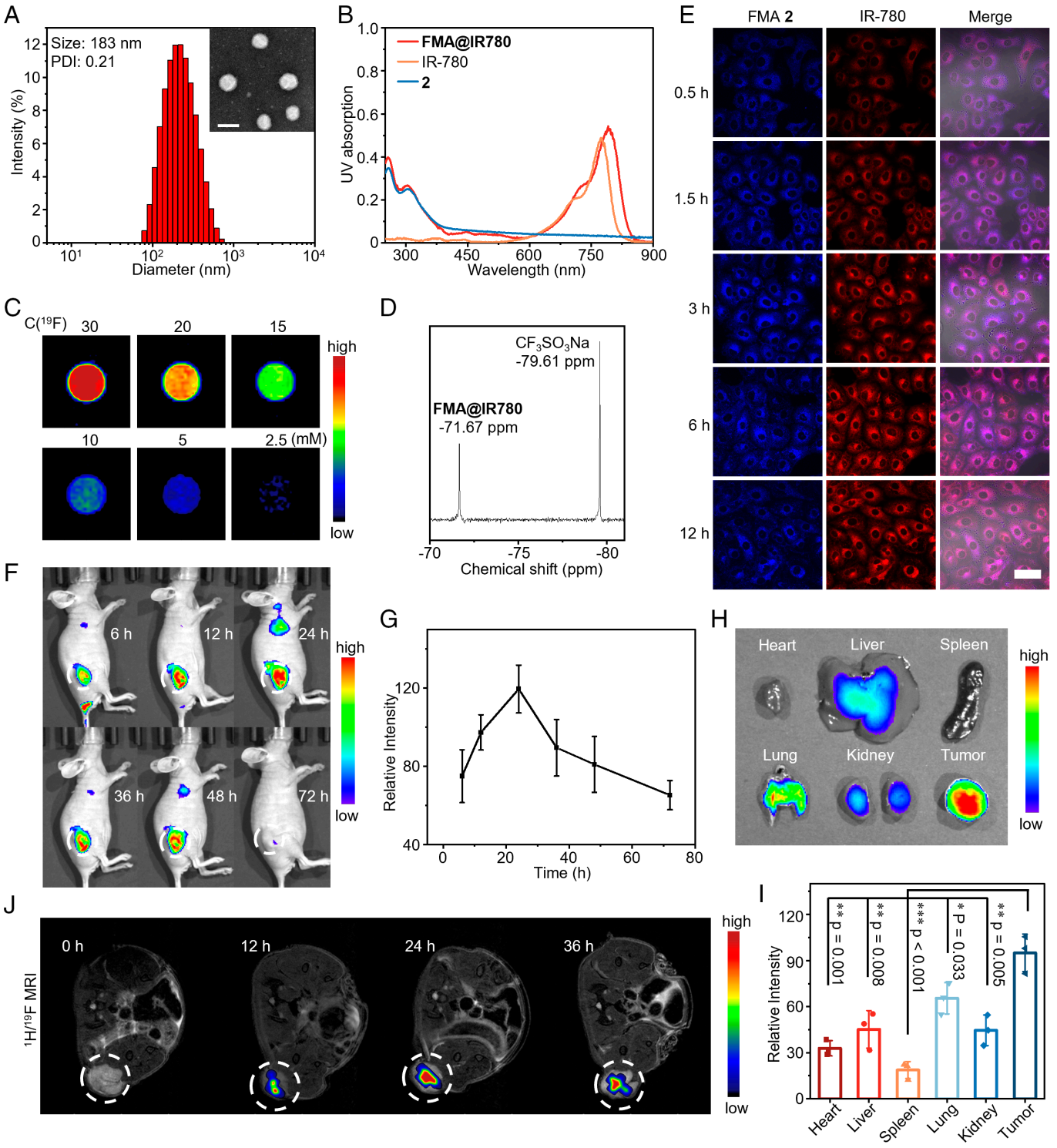

Fig. 5. DLS with insert TEM image of **FMA@IR780** (*A*, scale bar: 200 nm), UV-Vis absorption spectra of **FMA@IR780**, FMA **2** and IR-780 (*B*), ^{19}F MRI phantom images of **FMA@IR780** at the indicated ^{19}F concentrations (*C*), ^{19}F NMR spectra of A549 cells after incubation with **FMA@IR780** for 24 h (*D*), confocal microscopy images of A549 cells after incubation with **FMA@IR780** at the indicated time points (*E*, scale bar: 50 μm), whole-body NIR FLI (*F*) and relative SI in the tumor regions (*G*) of BALB/c nude mice carrying xenograft A549 tumor at the indicated times after intravenous injection of **FMA@IR780**, NIR FLI (*H*) and relative SI (*I*) of internal organs and tumor collected 24 h postinjection, ^{19}F MRI of BALB/c nude mice carrying xenograft A549 tumor at the indicated times after intravenous injection of **FMA@IR780** (*J*). Groups of 3 mice were used in all cases. The asterisks indicate the statistical significance between the internal organs and tumor, $*P < 0.05$, $**P < 0.01$, and $***P < 0.001$.

attributed to their proximity and the overlap of FMA **2**'s maximum FL emission peak with DOX's maximum UV absorption peak. Confirmation of FRET was further supported by a significant decrease in the FL lifetime (Fig. 6*E*). Further analysis via sharp singlet ^{19}F NMR peaks with consistent chemical shifts and ^{19}F relaxation times across varying DOX contents revealed that DOX was loaded around the TPE of FMA **2** rather than around the PFTB groups (*SI Appendix*, Fig. S9). Additionally, **FMA@DOX** demonstrated sensitive and quantitative ^{19}F MRI at a low ^{19}F concentration of 5 mM, exhibiting a linear relationship between the logarithm of SI and the logarithm of ^{19}F concentration (Fig. 6*F* and *SI Appendix*, Fig. S5*B*). Moreover, the ratio of

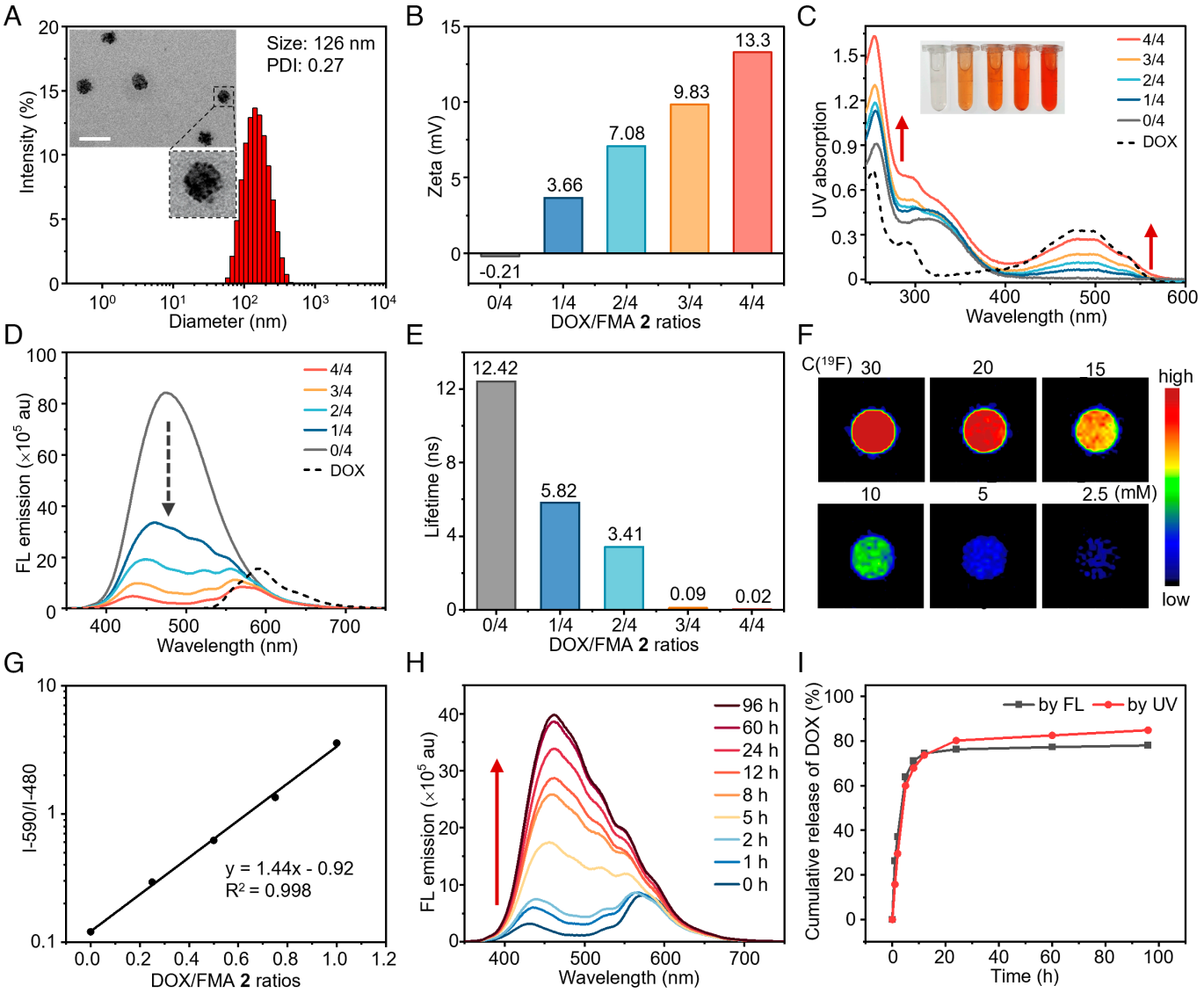

Fig. 6. DLS with insert TEM images of **FMA@DOX** (*A*, scale bar: 200 nm). Zeta potential (*B*), UV absorption spectra with insert images (*C*), FL emission spectra (*D*), and FL lifetime (*E*) of DOX-loaded nanoparticles with indicated DOX/FMA **2** molar ratios. ^{19}F MRI phantom images of **FMA@DOX** at the indicated ^{19}F concentrations (*F*), plot of the ratio of FL intensity at 590 nm and 480 nm against the loading of DOX (*G*), FL emission spectra during DOX release (*H*), DOX release curves (at pH 5.5) of **FMA@DOX** by FL and UV absorption methods (*I*).

FL intensities at 590 nm and 480 nm was directly proportional to the DOX content, facilitating convenient DOX quantification (Fig. 6*G*). Using a UV method, we measured the DOX entrapment efficacy and loading content of **FMA@DOX** as 90% and 8.8%, respectively. **FMA@DOX** exhibited a pH-dependent DOX release profile, with only 35% of DOX released at pH 7.4 and 94% at pH 5.5, enabling targeted release in acidic tumor tissues (*SI Appendix*, Fig. S10). Remarkably, the FL intensity of **FMA@DOX** changed during the drug release process and there was a high level of agreement observed in quantifying the DOX content of **FMA@DOX** using both ratiometric FL and UV absorption methods (Fig. 6 *H* and *I*). Therefore, the integrated use of FRET FL, ratiometric FL, and ^{19}F MRI presents a promising avenue for straightforward assessment of molecular drone drug delivery status, while simultaneously enabling precise tracking of its "hot spots".

The efficacy of imaging-guided delivery and therapy utilizing **FMA@DOX** was thoroughly investigated in both cancer cell cultures and xenograft tumor mice models. Notably, **FMA@DOX** exhibited moderately higher cytotoxicity toward A549 (IC_{50}: 1.8 ± 0.1 μM) and MCF-7 (IC_{50}: 4.7 ± 0.5 μM) cells compared to free DOX (IC_{50}: 2.2 ± 0.4 μM for A549, 8.5 ± 2.9 μM for MCF-7), indicating its proficient delivery of DOX into the targeted cells (Fig. 7*A* and *SI Appendix*, Fig. S6*B*). In A549 cells treated with **FMA@DOX**, a distinct single ^{19}F NMR fluorine peak was observed (Fig. 7*B*), further validated by confocal imaging which depicted the blue FL of FMA **2** within the cytoplasm and the green FL of DOX distributed in both the cytoplasm and nuclei (Fig. 7*C*). These findings affirm the successful intracellular delivery of DOX facilitated by **FMA@DOX**. The therapeutic efficacy of **FMA@DOX** was subsequently evaluated in BALB/c nude mice bearing A549 lung tumors of approximately 100 mm^3. Three groups of mice were intravenously administered phosphate-buffered saline (PBS), DOX, and **FMA@DOX** every 4 d, respectively (Fig. 7*D*). Tumor growth curves (Fig. 7*E*) and posttherapy tumor analysis (Fig. 7 *F* and *G*) revealed a significantly higher inhibition of tumor growth with **FMA@DOX** compared to DOX alone, with statistical significance. Remarkably, no signs of toxicity were observed during **FMA@DOX** therapy, and there was no notable loss in body weight among mice treated with **FMA@DOX** (Fig. 7*H*). Additionally, the histological hematoxylin and eosin (H&E) staining of internal organs collected after therapy, revealed

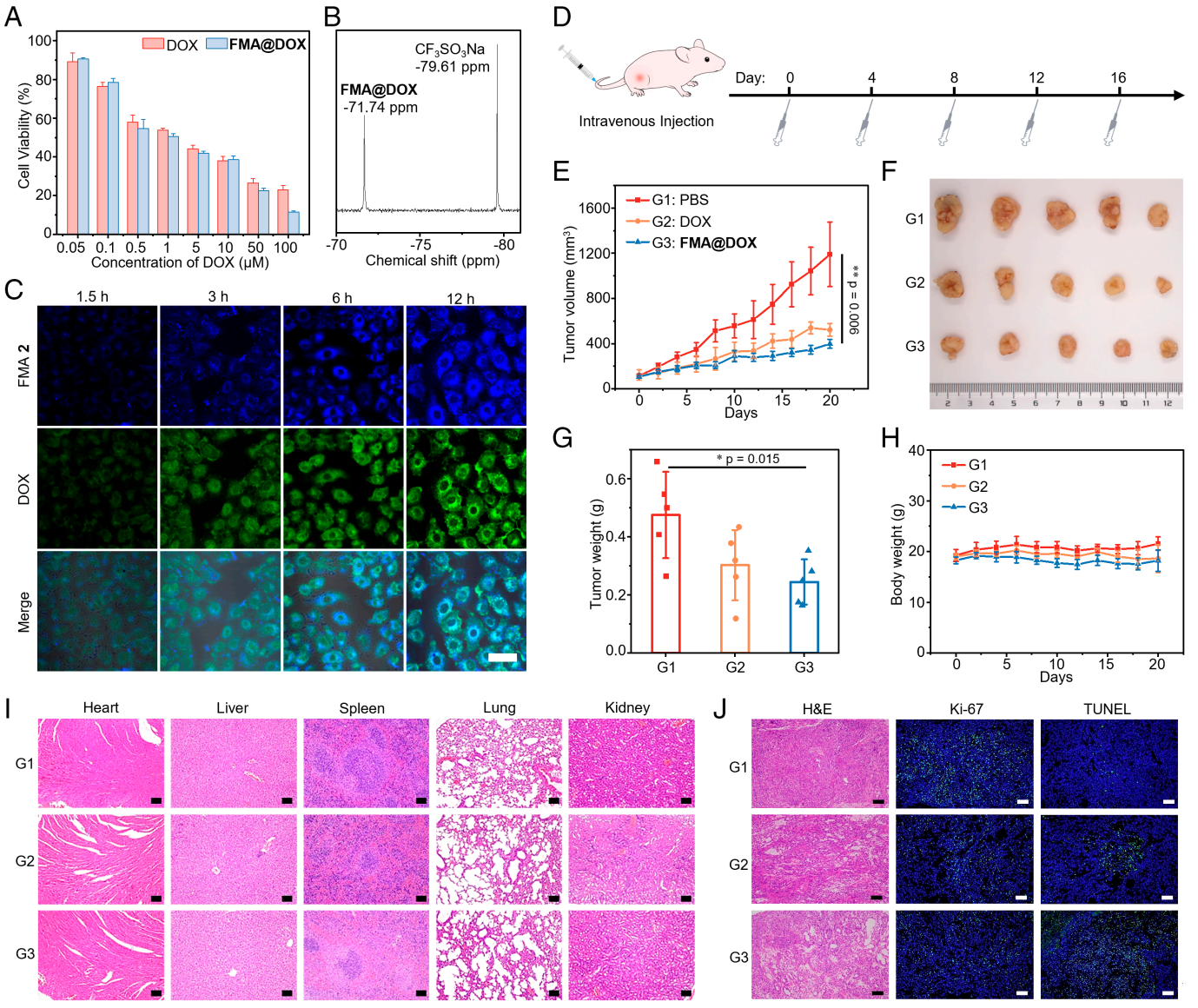

Fig. 7. Cytotoxicity assay of **FMA@DOX** and DOX toward A549 cells (*A*), ^{19}F NMR spectra (*B*), and confocal microscopy images (*C*, scale bar: 50 μm) of A549 cells incubated with **FMA@DOX**, schematic diagram of the therapeutic schedules (*D*), tumor growth curves (*E*) of the 3 groups of mice treated with PBS (G1), DOX (G2), and **FMA@DOX** (G3), respectively, photos (*F*), weight (*G*) of the tumors collected after the treatments and body weight curves of the 3 groups of mice (*H*). H&E staining of internal organs from G1, G2, and G3, scale bar: 100 μm (*I*). Representative H&E staining, Ki-67 staining, and TUNEL staining of tumor sections harvested from the mice receiving different treatments. Scale bars: 100 μm (*J*). Data were presented as mean ± SD (n = 5, the asterisks indicate the statistical significance between **FMA@DOX** and PBS, DOX, **P* < 0.05, ***P* < 0.01, and ****P* < 0.001).

no tissue abnormalities associated with **FMA@DOX** treatment (Fig. 7*I*). Obvious tissue damage was observed from the H&E staining of tumor sections harvested from the **FMA@DOX** treatment group (Fig. 7*J*). The terminal deoxynucleotidyl transferase (TdT)-mediated dUTP nick end labeling (TUNEL) staining of the tumor tissues showed the **FMA@DOX** caused the most severe tumor apoptosis by exhibiting the strongest TUNEL fluorescence, and the expressions of cell proliferation-related antigen Ki-67 were significantly downregulated in the tumor tissues from the **FMA@DOX** group, which further verified the antiproliferative activity of **FMA@DOX** (Fig. 7*J*). Therefore, FMA **2** demonstrates an efficient capacity to encapsulate DOX within stable and uniformly dispersed **FMA@DOX**, featuring pH-responsive DOX release, sensitive ^{19}F MRI, and real-time FL status reporting. These attributes enable the effective delivery of DOX into cancer cells and tumor regions, culminating in superior therapeutic outcomes.

Conclusions

In conclusion, our study demonstrates the successful development and application of fluorinated macromolecular amphiphiles as molecular drones for dual imaging-guided cargo loading, delivery, status reporting, and cancer diagnosis and therapy. Leveraging the unique properties of fluorinated macromolecular amphiphiles, including their high biocompatibility, stability, and multimodal imaging capabilities, we have engineered a versatile platform for targeted drug delivery, multimodal diagnosis, and real-time monitoring of therapeutic interventions. Through comprehensive in vitro and in vivo investigations, we have shown the efficacy of fluorinated macromolecular amphiphiles in loading therapeutic payloads such as the photosensitizer IR-780 and the chemotherapy drug doxorubicin, while simultaneously enabling ^{19}F MRI, Förster resonance energy transfer, and fluorescence imaging for accurate status reporting and tumor detection. Our results highlight the potential of

fluorinated macromolecular amphiphiles as promising candidates for precision medicine and theranostic applications in oncology.

The prospects of molecular drones in biomedicine are promising and multifaceted. Future research could focus on enhancing targeting strategies, expanding cargo diversity, incorporating smart stimuli-responsive systems, advancing imaging and monitoring techniques, optimizing biocompatibility and safety, validating in vivo efficacy, and translating findings into clinical applications. These efforts aim to realize the full potential of molecular drones for precision medicine, personalized therapy, and theranostics, offering tailored treatments based on individual patient profiles. Overall, interdisciplinary research endeavors hold the key to unlocking the transformative impact of molecular drones across various biomedical domains.

Materials and Methods

Detailed materials and methods are provided in *SI Appendix*, including all materials and instruments, chemical synthesis and characterization of fluorinated macromolecular amphiphiles, and all in vitro and in vivo biological assays. All experimental procedures involving animals strictly adhered to the Guideline for Animal Care and Use, Innovation Academy for Precision Measurement Science and Technology, Chinese Academy of Sciences (APM23042A). The mouse experimental protocols were conducted in accordance with the Regulations for the Administration of Affairs Concerning Experimental Animals, which were approved by the State Council of the People's Republic of China. Key techniques and protocols used in this manuscript are summarized below, with fully detailed descriptions present in *SI Appendix*.

Cell Culture. MCF-7 cells, MCF-10A cells, and A549 cells were procured from the Cell Bank of the Chinese Academy of Sciences (Shanghai, China). All cells were cultured in Dulbecco's Modified Eagle's Medium (DMEM) supplemented with 10% fetal bovine serum and 1% penicillin-streptomycin. The cells were maintained at a temperature of 37 °C in a humidified atmosphere containing 5% CO_2.

Animal Studies. Female BALB/c nude mice at the age of 5 wk were sourced from Beijing Vital River Laboratory Animal Technology Co., Ltd. (Beijing, China). The mice had free access to water and food until tumor size were large enough for the experiment. Mice were weighed regularly and killed at the indicated time points for tissue harvest.

Preparation of Nanoparticles. Nanoparticles loaded with different drugs were prepared using the solvent evaporation method with FMA **2**. The preparation process of **FMA@DOX** was presented as an example. First, 21.1 mg of FMA **2** and 2.2 mg of DOX were dissolved in an appropriate amount of DCM. Then, 4 mL of deionized water was added, and the mixture was emulsified by ultrasonication for 30 min. The final **FMA@DOX** nanoparticles were obtained by removing the residual DCM.

Data, Materials, and Software Availability. All study data are included in the article and/or *SI Appendix*.

ACKNOWLEDGMENTS. This work was supported by the Strategic Priority Research Program of the Chinese Academy of Sciences (XDB0540000), the National Key R&D Program of China (2018YFA0704000), the National Natural Science Foundation of China (22327901, 22077098, U21A20392, 21921004, and 82127802), the China Postdoctoral Science Foundation (2023M743583 and GZC20232754), the Knowledge Innovation Program of Wuhan-Basic Research (2022020801010137), and the Youth Innovation Promotion Association and the Young Top-notch Talent Cultivation.

Author affiliations: [a]State Key Laboratory of Magnetic Resonance and Atomic and Molecular Physics, National Center for Magnetic Resonance in Wuhan, Wuhan Institute of Physics and Mathematics, Innovation Academy for Precision Measurement Science and Technology, Chinese Academy of Sciences, Wuhan 430071, China; [b]School of Pharmaceutical Sciences, Wuhan University, Wuhan 430071, China; [c]Wuhan National Laboratory for Optoelectronics, Huazhong University of Science and Technology, Wuhan 430071, China; [d]University of Chinese Academy of Sciences, Beijing 100049, China; and [e]Key Laboratory of Organofluorine Chemistry, Shanghai Institute of Organic Chemistry, Chinese Academy of Sciences, Shanghai 200032, China

1. G. Yu *et al.*, Polyrotaxane-based supramolecular theranostics. *Nat. Commun.* **9**, 766 (2018).
2. X. Li *et al.*, Supramolecular phthalocyanine assemblies for improved photoacoustic imaging and photothermal therapy. *Angew. Chem., Int. Ed.* **59**, 8630–8634 (2020).
3. H.-T. Feng *et al.*, Substitution activated precise phototheranostics through supramolecular assembly of AIEgen and calixarene. *J. Am. Chem. Soc.* **142**, 15966–15974 (2020).
4. J. Li *et al.*, Supramolecular self-assembly-facilitated aggregation of tumor-specific transmembrane receptors for signaling activation and converting immunologically cold to hot tumors. *Adv. Mater.* **33**, 2008518 (2021).
5. J. Xu *et al.*, Metal-coordinated supramolecular self-assemblies for cancer theranostics. *Adv. Sci.* **8**, 2101101 (2021).
6. H. Cabral, N. Nishiyama, K. Kataoka, Supramolecular nanodevices: From design validation to theranostic nanomedicine. *Acc. Chem. Res.* **44**, 999–1008 (2011).
7. Z. Li *et al.*, Mesoporous silica nanoparticles in biomedical applications. *Chem. Soc. Rev.* **41**, 2590–2605 (2012).
8. A. Chen, S. Chatterjee, Nanomaterials based electrochemical sensors for biomedical applications. *Chem. Soc. Rev.* **42**, 5425–5438 (2013).
9. C. Chu *et al.*, Tumor microenvironment-triggered supramolecular system as an in situ nanotheranostic generator for cancer phototherapy. *Adv. Mater.* **29**, 1605928 (2017).
10. J. Zhou *et al.*, Supramolecular cancer nanotheranostics. *Chem. Soc. Rev.* **50**, 2839–2891 (2021).
11. W. R. Sanhai, J. H. Sakamoto, R. Canady, M. Ferrari, Seven challenges for nanomedicine. *Nat. Nanotechnol.* **3**, 242–244 (2008).
12. P. Satalkar, B. S. Elger, P. Hunziker, D. Shaw, Challenges of clinical translation in nanomedicine: A qualitative study. *Nanomedicine* **12**, 893–900 (2016).
13. K. Guidolin, G. Zheng, Nanomedicines lost in translation. *ACS Nano* **13**, 13620–13626 (2019).
14. I. Csoka, R. Ismail, O. Jojart-Laczkovich, E. Pallagi, Regulatory considerations, challenges and risk-based approach in nanomedicine development. *Curr. Med. Chem.* **28**, 7461–7476 (2021).
15. A. B. Chinen *et al.*, Nanoparticle probes for the detection of cancer biomarkers, cells, and tissues by fluorescence. *Chem. Rev.* **115**, 10530–10574 (2015).
16. A. L. Antaris *et al.*, A small-molecule dye for NIR-II imaging. *Nat. Mater.* **15**, 235–242 (2016).
17. L. Wu *et al.*, Reaction-based fluorescent probes for the detection and imaging of reactive oxygen, nitrogen, and sulfur species. *Acc. Chem. Res.* **52**, 2582–2597 (2019).
18. C. Li *et al.*, Advanced fluorescence imaging technology in the near-infrared-II window for biomedical applications. *J. Am. Chem. Soc.* **142**, 14789–14804 (2020).
19. X. Cai, B. Liu, Aggregation-induced emission: Recent advances in materials and biomedical applications. *Angew. Chem., Int. Ed.* **59**, 9868–9886 (2020).
20. J. Ruiz-Cabello, B. P. Barnett, P. A. Bottomley, J. W. M. Bulte, Fluorine (19F) MRS and MRI in biomedicine. *NMR Biomed.* **24**, 114–129 (2011).
21. I. Tirotta *et al.*, 19F magnetic resonance imaging (MRI): From design of materials to clinical applications. *Chem. Rev.* **115**, 1106–1129 (2015).
22. T. Wu *et al.*, Perfluoro-tert-butanol: A cornerstone for high-performance fluorine-19 magnetic resonance imaging. *Chem. Commun.* **57**, 7743–7757 (2021).
23. S. Mizukami *et al.*, Dual-function probe to detect protease activity for fluorescence measurement and 19F MRI. *Angew. Chem., Int. Ed.* **48**, 3641–3643 (2009).
24. S. Bo *et al.*, Design and synthesis of fluorinated amphiphile as 19F MRI/fluorescence dual-imaging agent by tuning the self-assembly. *J. Org. Chem.* **80**, 6360–6366 (2015).
25. H. Zhang *et al.*, 129Xe hyper-CEST/19F MRI multimodal imaging system for sensitive and selective tumor cells detection. *ACS Appl. Bio Mater.* **2**, 27–32 (2019).
26. R. T. Kadakia *et al.*, A dual-responsive probe for detecting cellular hypoxia using 19F magnetic resonance and fluorescence. *Chem. Commun.* **55**, 8860–8863 (2019).
27. Y. Li *et al.*, Multiresponsive nanoprobes for turn-on fluorescence/19F MRI dual-modal imaging. *Anal. Chem.* **92**, 11739–11746 (2020).
28. S. Wang, P. Huang, X. Chen, Stimuli-responsive programmed specific targeting in nanomedicine. *ACS Nano* **10**, 2991–2994 (2016).
29. T. Thambi, J. H. Park, D. S. Lee, Stimuli-responsive polymersomes for cancer therapy. *Biomater. Sci.* **4**, 55–69 (2016).
30. M. Karimi *et al.*, Smart nanostructures for cargo delivery: Uncaging and activating by light. *J. Am. Chem. Soc.* **139**, 4584–4610 (2017).
31. F. Li *et al.*, Stimuli-responsive nano-assemblies for remotely controlled drug delivery. *J. Controlled Release* **322**, 566–592 (2020).
32. V. Torchilin, Tumor delivery of macromolecular drugs based on the EPR effect. *Adv. Drug Delivery Rev.* **63**, 131–135 (2011).
33. J. Fang, H. Nakamura, H. Maeda, The EPR effect: Unique features of tumor blood vessels for drug delivery, factors involved, and limitations and augmentation of the effect. *Adv. Drug Delivery Rev.* **63**, 136–151 (2011).
34. F. Danhier, To exploit the tumor microenvironment: Since the EPR effect fails in the clinic, what is the future of nanomedicine? *J. Controlled Release* **244**, 108–121 (2016).
35. K. Ulbrich *et al.*, Targeted drug delivery with polymers and magnetic nanoparticles: Covalent and noncovalent approaches, release control, and clinical studies. *Chem. Rev.* **116**, 5338–5431 (2016).
36. Y. Wang *et al.*, Peptide-drug conjugates as effective prodrug strategies for targeted delivery. *Adv. Drug Delivery Rev.* **110-111**, 112–126 (2017).
37. J. Zhou, J. Rossi, Aptamers as targeted therapeutics: Current potential and challenges. *Nat. Rev. Drug Discovery* **16**, 181–202 (2017).
38. Y. Hong, J. W. Y. Lam, B. Z. Tang, Aggregation-induced emission. *Chem. Soc. Rev.* **40**, 5361 (2011).
39. J. Mei *et al.*, Aggregation-induced emission: Together we shine, United we soar! *Chem. Rev.* **115**, 11718–11940 (2015).
40. J. Zhu *et al.*, Peptidic monodisperse PEG "comb" as multifunctional "add-on" module for imaging-traceable and thermo-responsive theranostics. *Adv. Healthcare Mater.* **9**, 1901331 (2020).
41. H. Zhang *et al.*, Fluorinated porphyrin-based theranostics for dual imaging and chemo-photodynamic therapy. *J. Mater. Chem. B* **8**, 4469–4474 (2020).

42. H. Zhang *et al.*, Fluorinated cryptophane-A and porphyrin-based theranostics for multimodal imaging-guided photodynamic therapy. *Chem. Commun.* **56**, 3617–3620 (2020).
43. Y. Zheng *et al.*, Jellyfish-inspired smart tetraphenylethene lipids with unique AIE fluorescence, thermal response, and cell membrane interaction. *J. Mater. Chem. B* **12**, 2373–2383 (2024).
44. H. Zhang *et al.*, Highly efficient synthesis of monodisperse poly (ethylene glycols) and derivatives through macrocyclization of oligo (ethylene glycols). *Angew. Chem., Int. Ed.* **54**, 3763–3770 (2015).
45. G. Xia, Y. Li, Z. Yang, Z.-X. Jiang, Development of a scalable process for α-amino-ω-methoxyl-dodecaethylene glycol. *Org. Process Res. Dev.* **19**, 1769–1773 (2015).
46. J. Zhang *et al.*, Synthesis of branched monodisperse oligoethylene glycols and 19F MRI-traceable biomaterials through reductive dimerization of azides. *J. Org. Chem.* **85**, 6778–6787 (2020).
47. C. Li *et al.*, A general strategy to construct fluorogenic probes from charge-generation polymers (CGPs) and AIE-active fluorogens through triggered complexation. *Angew. Chem., Int. Ed.* **51**, 455–459 (2012).
48. H. Iijima, S. Koyama, K. Fujio, Y. Uzu, NMR study of the transformation of perfluorinated surfactant solutions. *Bull. Chem. Soc. Jpn.* **72**, 171–177 (1999).
49. P. Florence, I. Ilias, Aggregation mechanism of amphiphilic associating polymers studied by 19F and 13C nuclear magnetic resonance. *J. Phys. Chem. B* **103**, 4803–4808 (1999).
50. M. C. A. Stuart, J. C. van de Pas, J. B. F. N. Engberts, The use of Nile Red to monitor the aggregation behavior in ternary surfactant-water-organic solvent systems. *J. Phys. Org. Chem.* **18**, 929–934 (2005).
51. Z. Feng *et al.*, Flexible and zwitterionic fluorinated hydrogel scaffold with high fluorine content for noninvasive 19F magnetic resonance imaging under ultrahigh scanning resolution. *Adv. Healthcare Mater.* **12**, e2201894 (2023).
52. Y. Mo *et al.*, Recent research progress of 19F magnetic resonance imaging probes: Principle, design, and their application. *Macromol. Rapid Commun.* **44**, e2200744 (2023).
53. M. Iqbal, N. Zafar, H. Fessi, A. Elaissari, Double emulsion solvent evaporation techniques used for drug encapsulation. *Int. J. Pharm.* **496**, 173–190 (2015).